Available online at www.sciencedirect.com

ScienceDirect

Advances in Space Research 75 (2025) 2289–2306

ADVANCES IN SPACE RESEARCH (a COSPAR publication)

www.elsevier.com/locate/asr

Potential of non-flat solar sail for higher characteristic acceleration

Letícia Santos Lula Barros [a,*], Koju Hiraki [a], Marcelo Assis da Silveira [b], Yew-Chung Chak [c], Amirul Fiqri Abdullah [c], Renuganth Varatharajoo [c]

[a] *Kyushu Institute of Technology, Kitakyushu 8048550, Japan*
[b] *Independent Researcher, Brazil*
[c] *Universiti Putra Malaysia, Department of Space Engineering, Serdang 43400, Malaysia*

Received 22 July 2024; received in revised form 10 November 2024; accepted 15 November 2024
Available online 26 November 2024

Abstract

Solar sails offer a promising means of propelling spacecraft by harnessing Solar Radiation Pressure. Although non-flat solar sails have traditionally been considered less efficient in generating thrust, altering the sails' design to a non-flat configuration can enhance structural stability, allowing for thinner sail films and reducing overall mass. Consequently, non-flat sails could enable the use of larger sails for future space exploration without excessive mass. This study comprehensively explores non-flat solar sails using three folding techniques: Miura-Ori, Iso-area flasher by Palmer-Shafer, and Parachute-folded. The main goal is to optimize the characteristic acceleration while maintaining its structural integrity. Using Finite Element Analysis (FEA), we analyze deformation patterns and thrust generation to identify the most effective folding technique for a non-flat solar sail. The Parachute-folded sail with five support points demonstrated significantly improved the characteristic acceleration while maintaining a lower deformation than the other two folded configurations and the flat sail counterpart. Further, an enhancement was achieved by strategically integrating a polyimide reinforcement layer along its outer borders, resulting in a sail model with a higher structural resistance to deformation and decreased moment reaction compared to the uniform thickness Parachute-folded sail. Due to computational limitations, the thickness evaluated for this analysis was made in the interval of 30 μm to 400 μm. Investigating new solar sail designs can make large sails more feasible for future missions that are capable of shorter transfer times.

Keywords: Solar sail; Characteristic acceleration; Fold pattern; Space exploration; Low thrust propulsion

1. Introduction

Solar sails utilize Solar Radiation Pressure (SRP) to propel spacecraft, eliminating the need for traditional propellants like those used in chemical propulsion (McInnes, 1999; Vulpetti et al., 2008). This innovative technology offers the potential for long-duration missions to remote locations inaccessible to conventional propulsion systems. However, achieving the high characteristic acceleration required for rapid orbital maneuvers remains challenging for solar sails (Dachwald, 2010).

The performance of a sail is influenced by its area-to-mass ratio and deployment efficiency. A crucial stage is the change from a small, stowed configuration to a huge, fully deployed structure (Price et al., 2001; Baculi, 2016). This step requires a careful examination of the design options for larger solar sails that prioritize deformation resistance and lightweight construction.

Solar sails have advanced significantly with the success of missions like IKAROS, NanoSail-D2, and LightSail 2.

* Corresponding author.
E-mail addresses: leticiaslbarros@gmail.com (L. Santos Lula Barros), hiraki.koju735@mail.kyutech.jp (K. Hiraki), marcelosilveira.assis@gmail.com (M. Assis da Silveira), samchak11@gmail.com (Y.-C. Chak), amirulfiqriabdullah@gmail.com (A.F. Abdullah), renu99@gmx.de (R. Varatharajoo).

https://doi.org/10.1016/j.asr.2024.11.041
0273-1177/

With a massive 14 × 14 m sail, IKAROS was the first interplanetary solar sail launched in 2010 (Choi, 2015). Despite its impressive size, IKAROS may not be as suitable for missions requiring precise attitude control and sail rigidity due to its spinning configuration, which is needed for the lack of booms.

NanoSail-D2, deployed in 2011, and LightSail 2, launched in 2019 (Spencer et al., 2020), showed controlled solar sailing in Earth's orbit. Like many others, these missions have mainly employed a flat square sail form, common in solar sail technology.

Recent missions like NASA's NEA Scout and Solar Cruiser have demonstrated the challenges of setting up big, flat solar sails in space. Shortly after launch, NEA Scout, a CubeSat with an 85-square-meter solar sail, experienced communication problems that limited its ability to function (Zhao et al., 2023). Despite extensive ground tests, the Solar Cruiser mission was eventually canceled due to scheduling and technological constraints, despite its ambitious 1653-square-meter sail supported by four 30-meter-long booms (Johnson et al., 2023; Sikes et al., 2024). These examples show how urgently innovative approaches are required to overcome the barriers of deploying solar sails on a large scale.

Over time, research on the deployment of solar sails has evolved significantly. Early research focused on fundamental methods such as bistable booms and centrifugal deployment. The dynamics of the hexagonal membrane were investigated using numerical simulations by Okuizumi and Yamamoto (2009), and bistable booms were included to guarantee stable unfolding in space Fernandez et al. (2011).

Shape memory alloys (SMAs) transformed the field by greatly increasing deployment efficiency and dependability. Boschetto et al. (2019) and Bovesecchi et al. (2019) examined the application of SMAs for large-scale solar sails. More recent studies have concentrated on sophisticated strategies like force-based deployment, pre-tensioning, and creative folding techniques. Wang et al. (2024) used SMA springs for stress maintenance while examining how temperature changes affected solar sail deformation. Furthermore, Kezerashvili and Kezerashvili (2024) suggested a theoretical deployment strategy that combines pressurized gas, electric, and magnetic forces.

Innovations in large-scale sail deployment include ultralight deployable booms to mitigate bending and deformation issues Block et al. (2011), as well as the GOSSAMER project's Boom Sail Deployment Units (BSDUs), which ensure synchronized deployment and transition to wireless communication post-deployment (Grundmann et al., 2017). Parque et al. (2021) introduced a multi-spiral folding technique for flat and curved membranes, improving deployment, especially for curved surfaces Parque et al. (2021).

The concept of a solar power sail has emerged to explore the potential of solar sail technology further. Unlike traditional solar sails, which rely solely on sunlight reflection for propulsion, solar power sails integrate photovoltaic cells into the membrane to generate electricity. This dual functionality enables the sustainability of onboard systems, making them suitable for long-duration missions. However, adding solar cells increases the sail's thickness to around 200 μm, significantly thicker than conventional solar sails.

While large-scale demonstrations of solar power sails are still under development, the proposed OKEANOS mission by JAXA is a significant step in this direction. This mission aims to utilize a solar power sail to explore Trojan asteroids, showcasing the potential of this technology for future space exploration. (Takao et al., 2021).

Despite being the most common type, flat sails provide challenges for larger structures. Long, deployed masts are difficult to regulate and prone to bending under the stress of sun radiation. Even flat sails can exhibit unexpected deformations, as demonstrated in IKAROS, where the sail's ultimate shape was changed by the attached solar cells and control devices (Satou et al., 2014). However, this non-flatness could change the stiffness and sail designs in the future (Satou et al., 2015).

To get around these limitations, designs for non-flat solar sails have been created. They frequently feature shorter lever arms because they reliably distribute stress, which increases stability and reduces deformation. For instance, according to Berthet and Suzuki (2023), non-flat sails with pyramidal shapes can passively adjust their attitude using the torque produced by solar radiation pressure (SRP). In addition, non-flat sails are suggested by Miguel and Colombo (2021) for faster spacecraft deorbiting.

This paper explores alternative sail designs that leverage origami patterns to achieve a final non-flat configuration. We aim to minimize deformation on solar sails through an innovative design while delivering a good performance in characteristic acceleration. We examined designs that work effectively with square sails on booms, such as the Miura-Ori, Palmer-Shafer flasher, and Parachute-folded sail. Our approach investigates a non-flat design that preserves some folding in the final deployment stage, intending to strike a balance between thrust and stability. Comparable to IKAROS, we consider a sail size of 14 × 14 square meters to pave a new sail shape for larger solar sails.

Convergence is complex in simulations with thinner sails (e.g., less than 30 μm) because of intricate boundary conditions, including the distribution of support points and the effects of SRP. In addition, effective reinforcing techniques are crucial to preserving structural stability and minimizing deformation. Tension cables or the addition of strengthening materials along crucial edges can significantly impact how a sail behaves after deployment. These factors are essential for making precise performance estimates and ensuring that the sails can tolerate the stresses associated with sailing. This study explores non-flat sail designs and their potential to maximize performance while reducing deformation and structural instability.

2. Ideal reflection model for flat and folded configuration

In the ideal scenario of an optical surface, the Solar Radiation Pressure (SRP) force on a solar sail is influenced by the incident angle α, which is the angle between the plane normal vector $\hat{n}$ and the Sun's ray vector $\hat{s}$. This force arises from the momentum absorbed by incoming photons and the reaction provided by reflected photons. According to the law of reflection, which states that the angle of incidence equals the angle of reflection, the force vector of the SRP is always perpendicular to the surface plane of the sail, as shown in Fig. 1 (Dachwald, 2010; Choi, 2015).

The effective reflective area A and the pressure P due to SRP (Eq. (1)) is proportional to the force generated $\vec{f}$, corresponding to thrust. Here, $\vec{f}_s$ represents the thrust component due to incident rays, and $\vec{f}_r$ is the thrust component due to the reflected rays.

$$\vec{f}_s = PA(\hat{s}\cdot\hat{n})\hat{s} \tag{1}$$

The term $(\hat{s}\cdot\hat{n})\hat{s}$ denotes the projection of the reflective surface in the direction of $\hat{s}$. Similarly, Eq. (2) is expressed as:

$$\vec{f}_r = -PA(\hat{s}\cdot\hat{n})\hat{r} \tag{2}$$

Applying the vector identity, we derive the following Eq. (3):

$$\hat{r} - \hat{s} = 2(\hat{s}\cdot\hat{n})\hat{n} \tag{3}$$

The total thrust $\vec{f}$ is obtained by summing up both thrust components in Eq. (4):

$$\begin{aligned}\vec{f} &= \vec{f}_s + \vec{f}_r = PA(\hat{s}\cdot\hat{n})\hat{s} - PA(\hat{s}\cdot\hat{n})\hat{r} \\ &= -PA(\hat{s}\cdot\hat{n})(\hat{r}-\hat{s})\end{aligned} \tag{4}$$

Substituting Eq. 3 into Eq. 4, we arrive at Eq. 5:

$$\vec{f} = -2PA(\hat{s}\cdot\hat{n})(\hat{s}\cdot\hat{n})\hat{n} \tag{5}$$

Alternatively, the thrust $\vec{f}$ can be expressed as shown in Eq. (6), utilizing the dot product $a\cdot b = ab\cos\alpha$:

$$\vec{f} = -2PA(\cos\alpha)^2\hat{n} \tag{6}$$

The sail efficiency parameter η is a critical factor in a simplified SRP model, representing the efficiency of the sail's reflection capability, accounting for factors such as non-perfect reflectivity, wrinkles, and deformations. A higher η indicates more effective propulsion by reflecting a more significant number of solar photons, while a lower η reduces the thrust due to less efficient conversion of solar radiation. Optimizing η is crucial for designing efficient solar sails for compelling space exploration, with the SRP force expressed as shown in Eq. (7).

$$\vec{f} = 2\eta PA(\cos\alpha)^2\hat{n} \tag{7}$$

Increasing the characteristic acceleration (a_c), which is the greatest acceleration possible at a distance of 1 AU, is essential to optimizing a solar sail's performance. The sail normal vector is aligned with the sun rays for an optimal thrust, resulting in an angle α of zero. The characteristic acceleration is determined by the ratio of the sail area (A) to the total mass (m), as described by Eq. 8, where $f_{0,\max}$ is the maximum thrust at 1AU (Dachwald, 2010).

$$a_c = \frac{f_{0,\max}}{m} = \frac{2\eta P_0 A}{m} \tag{8}$$

2.1. Folded Sail

Non-flat solar sails can generate thrust components through reflection between adjacent panels, depending on their angles. Performance optimization requires consideration of energy dissipation and thrust components in undesired directions. The setup with two adjacent panels is shown in Fig. 2, where $\hat{s}$ is the unit vector in the direction of the Sun rays, and $\hat{r_1}$ and $\hat{r_2}$ are the unit vectors of the sun rays reflected from panels 1 and 2, respectively.

The thrust solely from the incident and reflected rays acting exclusively on panel 1 is denoted as $\vec{f}_{\text{srp1}}$. This can be expressed by components $\vec{f}_{s1}$ and $\vec{f}_{r1}$, defined in Eqs. 9 and 10, respectively. This approach is similar to the calculation for a flat sail shown in Eqs. (1)–(6), the resultant thrust $\vec{f}_{\text{srp1}}$ is the sum of $\vec{f}_{s1}$ and $\vec{f}_{r1}$, as shown in Eq. 11. In Fig. 2 the thrust for the first panel is denoted as $\vec{f}_1$ (Eq. 17) because it included the $\vec{f}_{\text{srp1}}$ component, which is present for the calculations of the ideal SRP (first incident and reflected rays). It includes the extra reflection component $\vec{f}_{12}$ that can exist due to the adjacent panel.

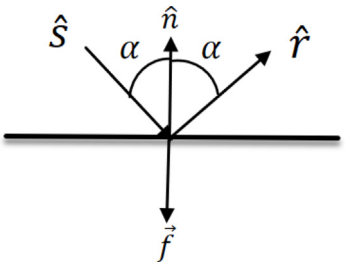

Fig. 1. Ideal reflection model.

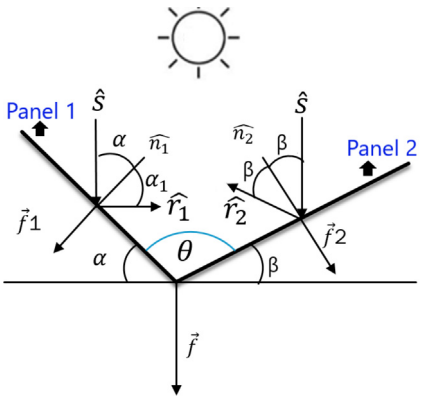

Fig. 2. Ideal reflection model for two panels.

$$\vec{f}_{s1} = PA_1 \cos\alpha\hat{s} \tag{9}$$

$$\vec{f}_{r1} = PA_1 \cos\alpha\hat{r}_1 \tag{10}$$

$$\vec{f}_{\text{srp1}} = 2 \cdot P \cdot A_1 \cdot \cos^2(\alpha)\hat{n}_1 \tag{11}$$

Similarly, for panel 2, the thrust components are given by Eqs. (12)–(14):

$$\vec{f}_{s2} = PA_2 \cos\beta\hat{s} \tag{12}$$

$$\vec{f}_{r2} = PA_2 \cos\beta\hat{r}_2 \tag{13}$$

$$\vec{f}_{\text{srp2}} = 2 \cdot P \cdot A_2 \cdot \cos^2(\beta)\hat{n}_2 \tag{14}$$

These Eqs. describe the components of thrust for each panel, where P is the pressure due to solar radiation, A_1 and A_2 are the areas of panels 1 and 2, α and β are the angles of incidence for panels 1 and 2 respectively, and $\hat{s}, \hat{r}_1, \hat{r}_2, \hat{n}_1$, and $\hat{n}_2$ are unit vectors indicating the directions of solar pressure, reflected rays, and normal to the panels.

2.1.1. Extra reflections

For $\theta < 120°$, if $\alpha + \beta > 60°$, the incident angle of the reflection can be calculated. The angle between the reflected ray and the panel normal vector can be determined using:

$$\beta_{12} = 180° - \alpha - 2\beta \tag{15}$$

The thrust component $\vec{f}_{12}$ on panel 1 due to the reflection from panel 2 is:

$$\vec{f}_{12} = 2\left|\vec{f}_{r2}\right| \cdot \cos^2(\beta_{12})\hat{n}_1 \tag{16}$$

The total thrust on panel 1 is then:

$$\vec{f}_1 = \vec{f}_{\text{srp1}} + \vec{f}_{12} \tag{17}$$

Similarly, for panel 2, the relevant angles and thrust components are:

$$\alpha_{12} = 180° - \beta - 2\alpha \tag{18}$$

$$\vec{f}_{21} = 2\left|\vec{f}_{r1}\right| \cdot \cos^2(\alpha_{12})\hat{n}_2 \tag{19}$$

$$\vec{f}_2 = \vec{f}_{\text{srp2}} + \vec{f}_{21} \tag{20}$$

Accounting for additional reflections must be repeated depending on the angle θ.

For specific examples of different angles for symmetric folds, it is possible to observe the number of reflections in Fig. 3.

In the particular case of vertical incidence, as illustrated in Fig. 3a, each reflected ray leaves the structure following a single interaction with the membrane without experiencing additional reflections. Additional reflections are impossible when the reflected beam from one side of the fold is parallel to the opposite side of the valley.

However, in Fig. 3b, the first reflection might leave without reaching the opposing valley wall for a second reflection if the incident ray hits further down the fold. This example illustrates how different surface parts reflect at different counts, resulting in a progressive shift between reflection modes. In particular, depending on the incidence angle and surface position, certain parts only reflect the ray once, while others produce a second reflection.

A consistent single mode reflection is observed throughout the surface at certain boundary angles, such as 120° and 90°. Here, the reflection behavior is uniform, with all points reflecting the same number of times under a given illumination angle. In flatter folds with larger values of θ, shallow or grazing angles of incidence can still cause the

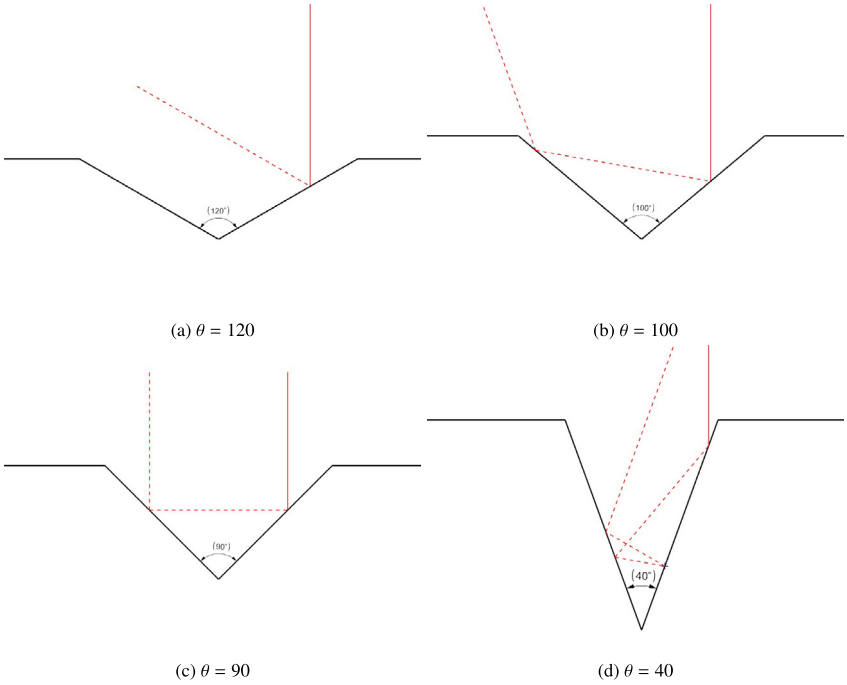

(a) θ = 120 (b) θ = 100

(c) θ = 90 (d) θ = 40

Fig. 3. Reflections for different values of θ.

first reflection to strike the opposite valley wall. This behavior is essential for solar sail applications, such as asteroid rendezvous missions, where regulated multi-reflection pathways improve mission feasibility and efficiency, especially at high grazing angles.

This study focuses mostly on near-vertical lighting angles to simplify multiple reflections. Although this approach limits the analysis to single or minimal reflections, additional reflections provide a promising direction for future research. For simplification, we present an approximate count of reflections by treating the number of reflections as discrete steps and disregarding the projected area that may contain extra reflections.

The number of reflections, N, can be determined using Eq. 21. This equation calculates reflections by considering only integer values and excluding the initial reflection, which is accounted for in preliminary calculations. The formula captures the maximum number of reflections before the angle becomes too steep, with results capped at six since additional reflections increasingly dilute the scattered component.

$$\mathrm{N} = \begin{cases} 0 & \text{if } \theta \geqslant 120^\circ \\ 1 & \text{if} 90^\circ \leqslant \theta < 120^\circ \\ \left\lfloor \frac{2\pi}{\theta_{rad}} - 1 \right\rfloor / 2 & \text{if } \theta < 90^\circ \end{cases} \tag{21}$$

Additional reflections are calculated separately for each panel. Furthermore, the number of reflections doubles, giving $2 \times \mathrm{N}$. Fig. 4 illustrates these additional reflections between panels for different combinations of α and β.

While step-wise, for individual surface elements, the transitions between reflection modes become nearly continuous across a larger membrane with fold valleys of limited height-to-width ratios. For such continuous membranes, the average number of reflections is more accurately represented as a continuous function rather than a strictly step-wise one.

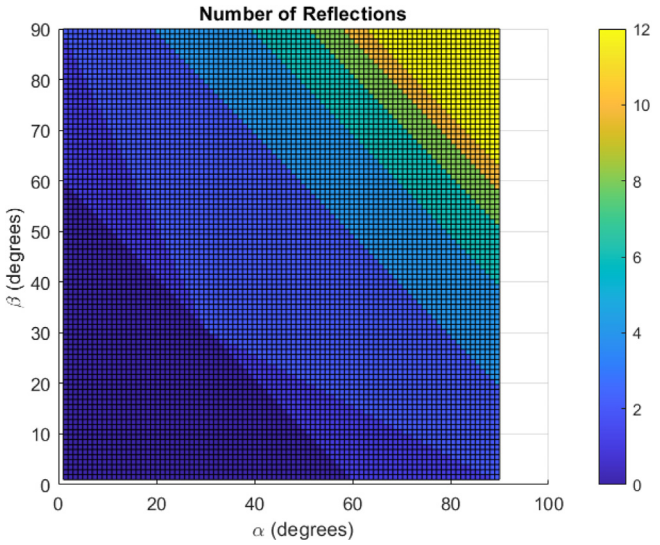

Fig. 4. Number of reflections.

In symmetric folds with vertical illumination, the horizontal thrust components generated by the fractional area reflection mode patterns cancel out. However, this may not be true for slant illumination and non-ideal surfaces. While this initial approach avoids the intricacies of double or multiple reflections, these effects represent a natural progression for future work.

Using two adjacent panels in solar sails can cause sunlight to reflect between them, potentially creating a localized temperature increase. These hot spots depend on factors such as the angle of sunlight and the geometry of the folding line, both of which are influenced by the tensile properties of the membrane (Seefeldt and Dachwald, 2020). Temperature also affects the electrical conductivity of the sail, which in turn influences its ability to reflect and absorb sunlight. As temperatures increase, conductivity decreases, requiring a thicker sail to maintain optimal performance (Kezerashvili, 2009). Furthermore, the structural stability of the sail is highly sensitive to temperature, as higher temperatures can compromise material integrity and durability Ancona and Kezerashvili (2017). This interplay between temperature, material properties, and sail geometry is the key to ensuring the structural integrity and efficiency of large-scale solar sails (Kezerashvili, 2009).

To account for the orientation of the panels relative to a reference direction, we decompose the thrust on each panel into its x and y components based on the angles α and β. We then sum these components to find the resulting vector $\vec{f}_{\text{total}}$.

$$\vec{f}_{\text{total}} = |\vec{f}_1| \begin{bmatrix} -\sin(\alpha) \\ \cos(\alpha) \end{bmatrix} + |\vec{f}_2| \begin{bmatrix} \sin(\beta) \\ \cos(\beta) \end{bmatrix} \tag{22}$$

We get the Eq. 23 to break this into components.

$$\vec{f}_{\text{total}} = \begin{bmatrix} -|\vec{f}_1| \sin(\alpha) + |\vec{f}_2| \sin(\beta) \\ |\vec{f}_1| \cos(\alpha) + |\vec{f}_2| \cos(\beta) \end{bmatrix} \tag{23}$$

The resultant thrust $\vec{f}_{\text{total}}$ is perpendicular to the sail if $\alpha = \beta$ (Eq. 24) as the vectors $|\vec{f}_1|$ and $|\vec{f}_2|$ would have the same module.

$$\vec{f}_{\text{total}} = \begin{bmatrix} 0 \\ |2\vec{f}_1| \cos(\alpha) \end{bmatrix} \tag{24}$$

Adjusting the panels' angles optimizes the solar sail's propulsion and control. By altering the fold angles, we can achieve a high thrust, achieving the desired direction and magnitude of propulsion for the spacecraft. Fig. 5 illustrates the estimated thrust for panels with various combination incident angles for panels with the same membrane area ($A_1 = A_2 = 1$ m^2), with the red marker highlighting the maximum thrust value obtained.

This thrust estimation assumes a single reflection mode per panel; in other words, it considers a uniform reflection count across each panel without accounting for any projected areas that might receive additional reflections.

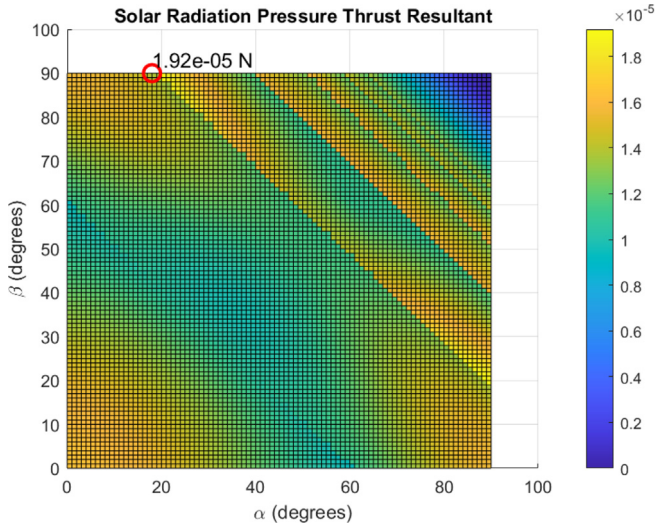

Fig. 5. Resulting Thrust from two adjacent panels with different incident angles in Newtons [N].

Different combinations of α and β can cause thrust in undesired directions. Fig. 6 shows the total thrust values when $\alpha = \beta$ is used to maintain a symmetrical fold and perpendicular thrust. The symmetrical fold achieves the maximum thrust when $\theta = 180$ degrees, indicating a flat sail. However, a high thrust value is observed around $\theta = 50$ degrees for a sail with multiple reflections. This curvature could be evaluated to reduce displacement while maintaining high thrust.

Since $\theta = 180 - (\alpha + \beta)$ and in a symmetrical fold $\alpha = \beta$, we can determine that α in that scenario is approximately 65 degrees.

Although there is potential to explore the use of multiple reflections between panels to achieve higher thrust, this study focused on a configuration where θ is large enough to avoid such reflections, thus preventing solar sail overheating. Specifically, we chose $\theta > 120^\circ$ to eliminate reflections between panels. Furthermore, we set α equal to β to produce symmetric thrust. Scattering effects may also become significant in the presence of non-ideal membranes and reflections. Expanding on this aspect using ray-tracing methods could be an exciting direction for future work.

$$\theta = 180 - 2\alpha > 120. \therefore \alpha < 30 \tag{25}$$

Fig. 7a shows a side view approximation of a non-flat solar sail, where D is the flat sail's side length ($\alpha = 0\circ$), N the number of folds, and h the fold height, calculated via Eq. 26. For a 14 m square sail, the full extension gives a diagonal length of $L = \sqrt{2} \times 14 = 19.8$ m, while partial extension reduces the projected area (Fig. 7b). The fold height (h) depends on N and the boom deployment percentage, approximated by Eq. 27. The ratio Booms/L represents boom deployment, with Booms $= L$ indicating 100% deployment, resulting in a flat sail.

$$h = \frac{D}{N} \sin \alpha \tag{26}$$

$$h \approx \frac{D}{N} \sin\left(\arccos\left(\frac{\text{Booms}}{L}\right)\right) \tag{27}$$

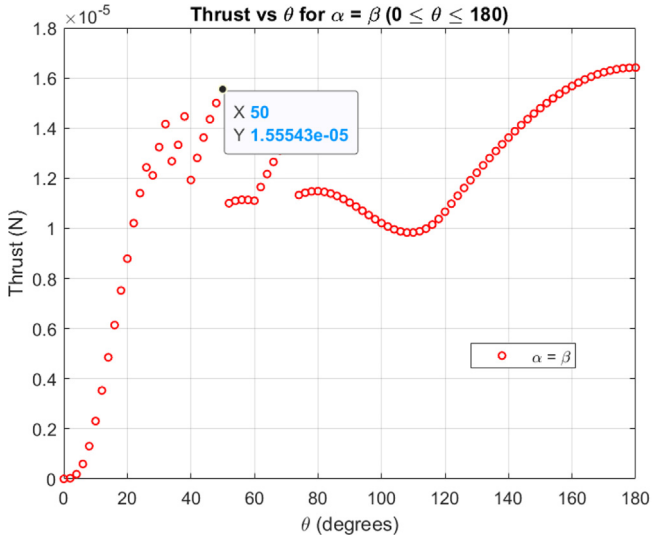

Fig. 6. Thrust for different angle θ between adjacent panels.

3. Folding techniques

Origami offers the ability to control flexibility and stiffness through crease patterns (Schenk and Guest, 2010). This characteristic can be exploited for deployable solar sails. Unlike traditional flat sails, origami designs can achieve the following:

- Adaptable shape: the capability to deform during deployment and operation while maintaining a taut surface for efficient interaction with solar radiation pressure (deformation anisotropy).
- Compact storage: Large deformations through fold opening and closing allow for compact storage during launch.
- Structural Integrity: The increased bending stiffness provided by the creases ensures functionality in space.

We focus on three promising origami folding techniques compatible with square sails and boom deployment.

3.1. Palmer-Shafer

The Palmer-Shafer folding technique, also known as the Iso-area flasher, illustrated in Fig. 8, was inspired by the Kawasaki iso-area twist folding. This fold employs a flasher design, which expands the sail material, resulting in a larger final area for the same initial volume. Closing the mechanism requires pushing it inward and turning counterclockwise, with the opposite movement needed for opening (Palmer and Shafer, 2004). This method primarily involves pulling vertices for deployment, making it compatible with the boom deployment approach. The Palmer-

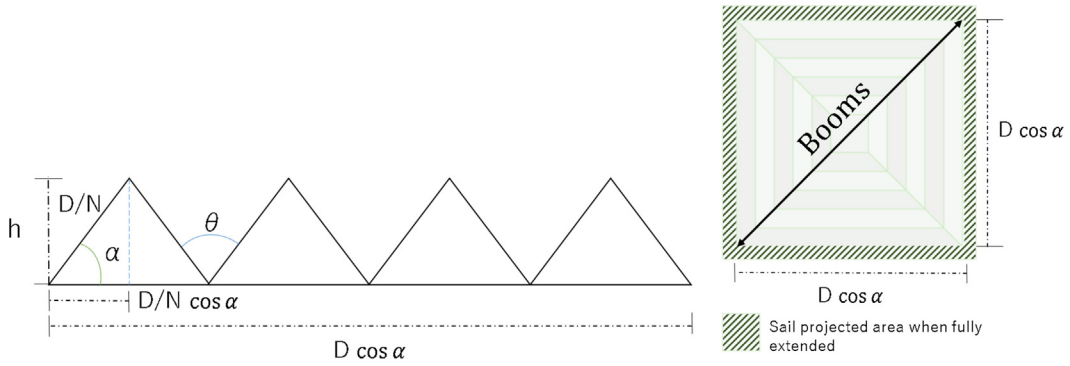

(a) Approximation of origami folds with inclined adjacent panels (b) sail partially folded, non-flat sail

Fig. 7. Origami-inspired folding and sail extension comparison.

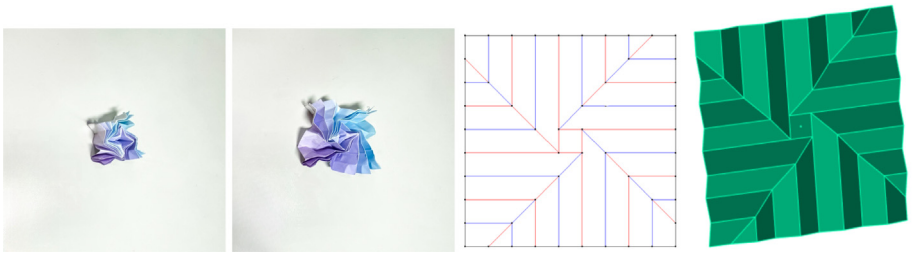

(a) Compact (b) Deploying (c) Fold design (d) 3D model

Fig. 8. Palmer-Shafer fold.

Shafer fold incorporates a series of right angles (Fig. 8c), providing enhanced stability and structural integrity, although it potentially requires more storage and deployment space than other techniques.

3.2. Miura-ori

The Miura-ori tessellated folding pattern has been introduced as an origami metamaterial. Initially, this design was created to optimize the packing of solar panels for space missions. (Silverberg et al., 2014) The Miura fold (Fig. 9) is a versatile origami zigzag pattern for sail panels, allowing compact storage suitable for missions with limited space. It ensures seamless deployment in a single motion, balancing efficient packing and deployability. In particular, only two vertices need to be pulled for deployment, eliminating the need for a four-boom configuration that requires only two booms.

3.3. Parachute-folded

The Parachute-folded pattern, illustrated in Fig. 10, involves folding the sail into concentric circles. This approach simplifies the initial folding of the sail edges around the central body of the spacecraft, as shown in Fig. 10a (Yo, 2021). The deployment of the Parachute-folded sail is based on extending the booms or rotating masses at the vertices.

Each folding approach can be tailored to meet the unique needs of different space missions. The choice of the folding pattern depends on factors such as available storage space, deployment mechanism, desired stability,

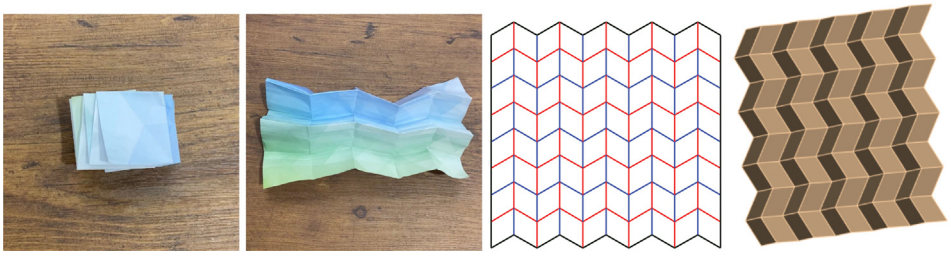

(a) Compact (b) Deploying (c) Miura pattern (d) 3D model

Fig. 9. Miura-ori.

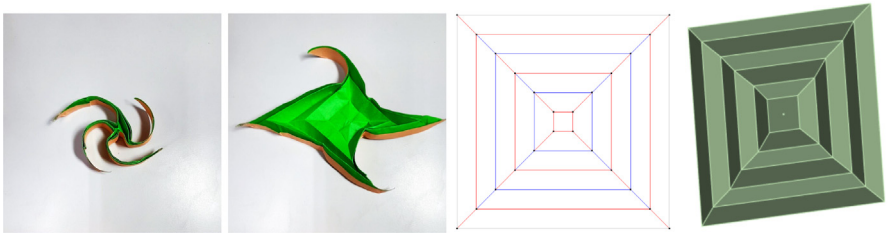

(a) Compact (b) Deploying (c) Fold pattern (d) 3D model

Fig. 10. Parachute-folded.

and structural integrity. Using these origami-inspired techniques, we can optimize the design and deployment of large square sails for their specific missions.

4. Software limitations in solar sail analysis

The analysis of solar sail membranes in this research was performed for thicknesses ranging from 30 μm to 400 μm. While these values are significantly thicker than the optimal specifications for pure solar sails, they align well with the thickness range anticipated for photovoltaic-integrated membranes. Precisely, a thickness of 400 μm corresponds to early demonstrator models, 200 μm aligns with the prototypes of larger-scale systems, and 30 μm matches the thin-film photovoltaic cells that can be directly deposited onto the main membrane. However, this study faced limitations due to the software used, which imposed constraints on computational capacity and model complexity. Despite these limitations, focusing on the single-reflection case within these parameters provides a feasible and relevant scope for initial analysis. These constraints, combined with the reasonable limits of this research, ensure the validity and applicability of the results within the context of developing hybrid solar-photovoltaic membranes.

Given these computational constraints, strategic reinforcement and folding techniques are essential to minimize deformation and optimize performance. To address the need for practical and efficient sail designs, the next stage of this study involves a detailed comparison of different fold patterns and their mechanical behavior under solar radiation pressure. By doing so, we aim to identify configurations that best balance the structural integrity and characteristic acceleration.

5. Fold patterns comparison

Our study investigates the deformation and thrust characteristics of three non-flat solar sails, each sharing identical thickness and material properties but employing distinct folding techniques. The sail was discretized into minor elements using Ansys Mechanical to apply support conditions, material properties, and solar radiation pressure as loads.

For the supports, a standard configuration with five support points (Fig. 11) was utilized, with the booms assumed to be rigid. Shell elements were employed to account for large deflections and accurately simulate the sail's behavior.

For simulations, we chose a maximum height of 0.5 m for all folds, resulting in a nearly full extension while maintaining an origami shape. The height values must be manageable; otherwise, we might not perceive a big difference in performance between the fold patterns. When summing all area segments, all models correspond to 196 m^2 for the total membrane area.

The number of folds varies for each fold due to their peculiarities. However, as shown in Fig. 12, the fraction of the side length ranges from $D/11$ to $D/9$, where D represents the total side length of the sail. These fractions are similar to maintain comparable side lengths for each segment. Moreover, these different fold patterns give each fold a unique incident angle α. Figs. 12a, 12b, and 12c show the side views of different origami folds. Modeling an accurate 3D representation of a partially opened origami is challenging. The folds are shown as flat, inclined adjacent panels to simplify our geometry. As a result, the height of each fold stays consistent.

For a folded height of $h = 0.5m$ and $D = 14m$, we calculate the values of $\frac{\text{Booms}}{L}$ for different numbers of folds N. These values and the corresponding boom extension percentages are shown below.

- For $N = 9 : \frac{\text{Booms}}{L} \approx 94.7\%$
- For $N = 10 : \frac{\text{Booms}}{L} \approx 93.4\%$
- For $N = 11 : \frac{\text{Booms}}{L} \approx 92.0\%$

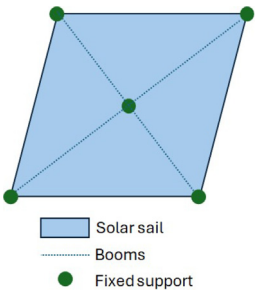

Fig. 11. Five-point connection configuration.

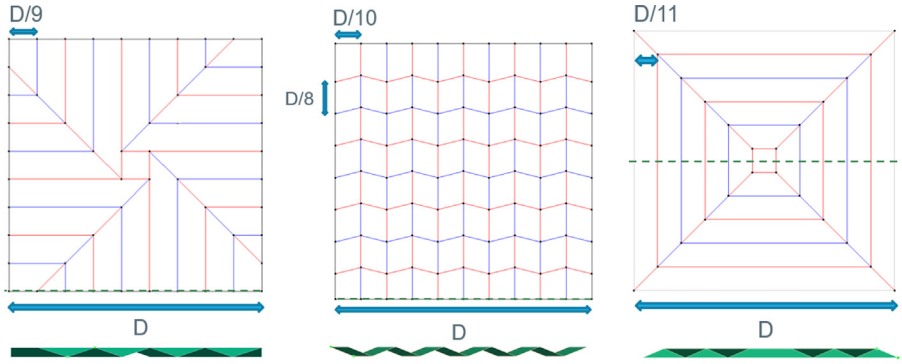

(a) Palmer Shaffer (b) Miura Ori (c) Parachute-folded sail

Fig. 12. Scheme of the folds applied to generate the 3D models.

All correspond to a boom extension of approximately 92.0% to 95.0%. It is important to note that these results are rough estimations based on the relationship between the fold height and the boom extension percentage. After designing the 3D models, we extracted the values, checked the matching membrane areas, and ensured consistent fold heights for a more accurate result.

To calculate the loads for each panel, we use the calculation of the ideal SRP to estimate the effective pressure to apply for the inclined segments. The effective Solar Radiation Pressure, P_{eff}, is computed as shown in Eq. 28 using an ideal model with a sail efficiency (η) of 0.9, based on the pressure at 1 AU, P_0.

Table 1
Effective pressure estimation.

Fold Technique	α	θ	P_{eff} [N/m^2]	Deployment %
Flat	0	180.00	8.22×10^{-6}	100
Palmer Shafer	17.52	144.95	7.37×10^{-6}	97
Miura Ori	21.00	138.00	7.18×10^{-6}	96
Parachute-folded	23.20	133.60	7.24×10^{-6}	96

Table 2
Sail film material properties.

Polyimide properties	
Density	1420 kg/m^3
Young modulus	3 GPa
Poisson Ratio	0.4

$$P_{\text{eff}} = 2 \cdot P_0 \cdot \eta \cdot \cos^2(\alpha) \tag{28}$$

The 3D design assumes consistent angles between adjacent panels to simplify the model. In addition, we kept $\theta > 120°$ to avoid reflection between panels. The effective pressure for different folding techniques is presented in Table 1, applied to the folded creases. We consider the equivalent pressure of a flat sail for creases perpendicular to the sun rays, such as the center of the Palmer-Shafer and Parachute-folded sail. We could obtain the incident angles and fold heights directly from the software for verification.

The material properties of the polyimide film, shown in Table 2, influence the selection and optimization of folding techniques. These properties are consistent with those of the IKAROS film (Shirasawa et al., 2012). Fig. 13 illustrates the meshing used in simulations for various patterns. The mesh size was adjusted to 0.2 meters, and finer details were set to 0.1 meters in certain areas to capture intricate features.

5.1. Average and maximum deformation

In this subsection, we analyze sails of equal area but with varied folding patterns to assess their deformation performance. Precisely, we measure the maximum and average displacements for different configurations: Flat, Palmer-Shafer, Miura-Ori, and Parachute-folded folds. Each pattern is tested with membrane thicknesses of 400 μm, 300 μm, and 200 μm, which are representative of photovoltaic membrane applications and aligned with current

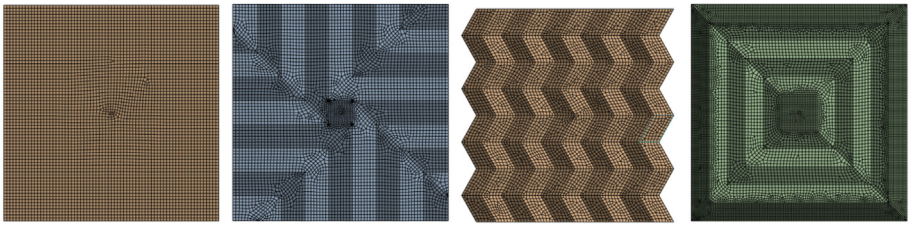

(a) Flat Sail (b) Palmer Shafer (c) Miura Ori (d) Parachute-folded

Fig. 13. Mesh used during the simulations.

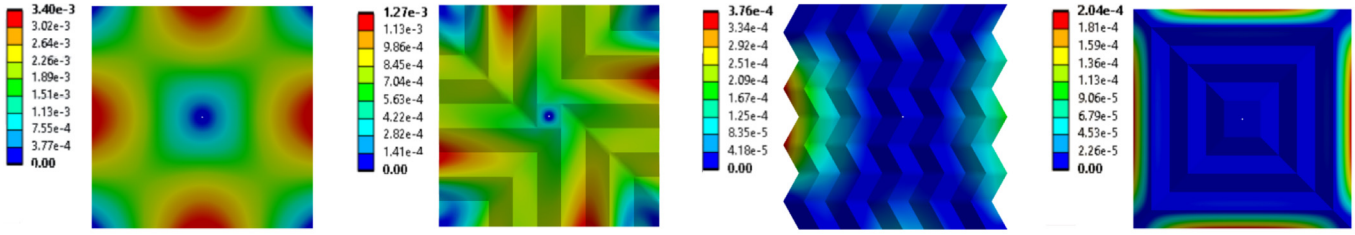

(a) Flat Sail (b) Palmer Shafer (c) Miura Ori (d) Parachute

Fig. 14. Deformation in meters due to P_{max} at $1AU$ on sails with five support points ($t = 400\ \mu m, A = 196\ m^2$).

and anticipated manufacturing capabilities. Furthermore, software limitations restricted some simulations to a membrane thickness of 30 μ m. This range helps to verify that the results obtained for membranes at least an order of magnitude thicker remain consistent and reliable.

5.1.1. Deformation for 400 μm Thickness

Fig. (14) illustrates the deformation patterns for the different folding configurations with 400 μm thickness. Table 3 presents the maximum and average deformation results.

The data in Table 3 show that all folded sails exhibit a reduced average deformation compared to the flat sail. The Miura-Ori fold demonstrates the least average deformation, suggesting an effective stress distribution. However, the Parachute-folded sail has the most negligible maximum deformation, indicating inherent stability under stress.

5.1.2. Deformation for 300 μm Thickness

Next, Fig. (15) shows the deformation of the folding patterns with a thickness of 300 μ m, and Table 4 provides the deformation data.

Table 3
Deformation at 1 AU on sails with a thickness of 400 μm, an area of 196 m^2, and a maximum height of 0.5 m.

	Maximum Deformation [m]	Average Deformation [m]
Flat Sail	3.40×10^{-3}	2.01×10^{-3}
Palmer Shafer	1.27×10^{-3}	6.63×10^{-4}
Miura Ori	3.76×10^{-4}	4.93×10^{-5}
Parachute-folded	2.04×10^{-4}	5.24×10^{-5}

Table 4
Deformation at 1 AU on sails with a thickness of 300 μm, an area of 196 m^2, and a maximum height of 0.5 m.

	Maximum Deformation [m]	Average Deformation [m]
Flat Sail	3.83×10^{-3}	2.28×10^{-3}
Palmer Shafer	3.00×10^{-3}	1.02×10^{-4}
Miura Ori	7.05×10^{-4}	8.92×10^{-5}
Parachute-folded	4.81×10^{-4}	6.06×10^{-5}

As shown in Table 4, the non-flat sails outperform the flat sail in reduced deformation. The Miura-Ori and Parachute-folded perform exceptionally well, with the Parachute-folded sail exhibiting symmetrical deformation patterns, which could minimize torque during deployment.

5.1.3. Deformation for 200 μm Thickness

Finally, Fig. 16 and Table 5 present the results for the thickness of 200 μm.

Now, for the results for the thickness 200 μm, the Palmer-Shafer presented a higher maximum deformation than the flat sail. Therefore, there might be an interval of thickness where each fold is stiffer than the flat sail. Based on those results, the Parachute-folded sail demonstrated better results across different thicknesses and was selected for future analysis.

5.2. Thrust comparison for sails of equal area and different folding techniques

In this study, we applied Solar Radiation Pressure (SRP), denoted by P, to solar sails with the same total sur-

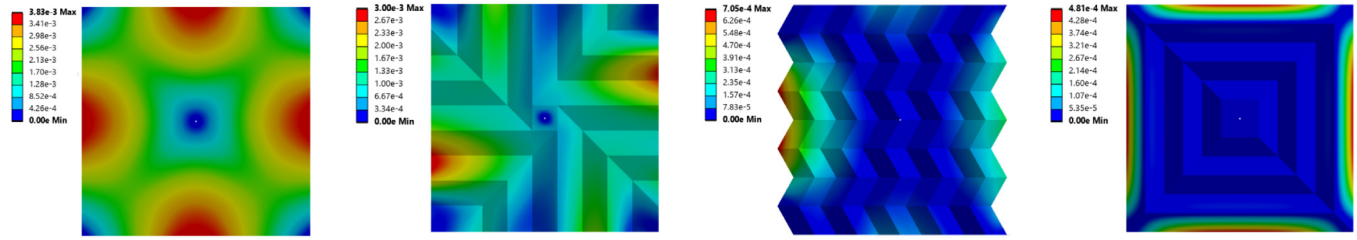

(a) Flat Sail (b) Palmer Shafer (c) Miura Ori (d) Parachute

Fig. 15. Deformation in meters due to P_{max} at $1AU$ on sails with five support points ($t = 300\ \mu m, A = 196\ m^2$).

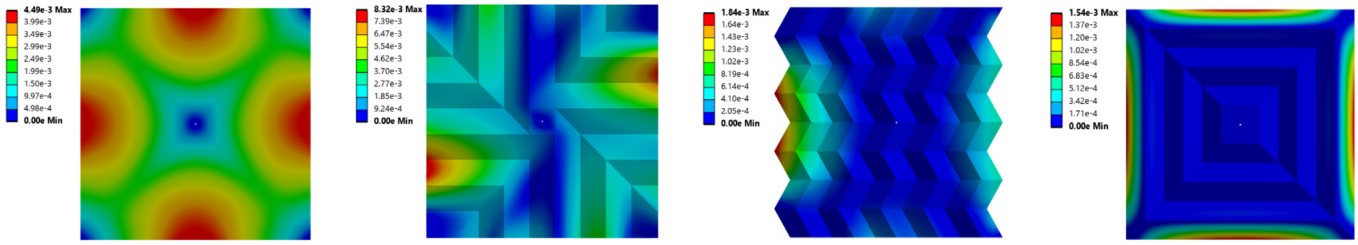

(a) Flat Sail (b) Palmer Shafer (c) Miura Ori (d) Parachute

Fig. 16. Deformation in meters due to $P_{\max}$ at $1AU$ on sails with five support points ($t = 200\ \mu m, A = 196\ m^2$).

Table 5
Deformation at 1 AU on sails with a thickness of 200 μm, an area of 196 m^2, and a maximum height of 0.5 m.

	Maximum Deformation [m]	Average Deformation [m]
Flat Sail	4.49×10^{-3}	2.69×10^{-3}
Palmer Shafer	8.32×10^{-3}	2.22×10^{-3}
Miura Ori	1.84×10^{-3}	2.22×10^{-4}
Parachute-folded	1.54×10^{-3}	1.85×10^{-4}

face area A to measure the generated thrust f. Due to the non-linear analysis, we based our calculations on the deformed shapes obtained from the previous subsection, accounting for bending and twisting, which can affect the area exposed to SRP.

Although all sails were analyzed at a distance of 1 AU from the Sun, the effective pressure on each sail panel varied based on its pitch angle α relative to the incoming solar rays, as discussed earlier. This variation in pitch angle affects the distribution of SRP across the sail, leading to differences in effective pressure and, consequently, in the resulting thrust. Panels with higher pitch angles experience reduced effective pressure, leading to a lower total thrust, even when the total sail area remains constant.

Table 6 presents the thrust results for different solar sail configurations using a support system with five connecting points. The table shows the absolute thrust for each sail design and the percentage of thrust relative to a flat sail, facilitating easier comparison of different geometries. This comparison highlights how folding patterns and pitch angles impact the total thrust generated by each configuration.

Table 6
Thrust at 1 AU for different fold patterns with a maximum fold height of 0.5 m, a total area of 196 m^2, and a thickness of 400 μm.

Fold	Thrust [N]	Thrust [% of Flat Sail]
Flat Sail	1.61×10^{-3}	100
Palmer Shafer	1.37×10^{-3}	85
Miura Ori	1.29×10^{-3}	80
Parachute-folded	1.31×10^{-3}	82

To simplify the analysis, we only report the thrust values for a sail thickness of 400 μm, as there was minimal variation in thrust between thicknesses ranging from 400 μm to 200 μm.

The expected total thrust for an ideal flat sail at 1 AU can be calculated using Eq. 29, where the result for the flat sail is consistent with the theoretical prediction. For non-flat sails, the total thrust decreases due to the inclination of the panels.

$$f_0 = P_{eff,0} \times A = 1.61 \times 10^{-3}\,\mathrm{N} \tag{29}$$

The results show that the Palmer-Shafer fold retains a higher percentage of thrust with a fold height of 0.5 m. However, considering the significant deformation noted in the earlier analysis, the Parachute-folded appears to be the most promising design for maintaining thrust in future investigations.

6. Investigating deformation for different fold angles using the parachute-folded sail

To further refine the Parachute-folded sail, we investigate how the angle θ (the angle between folds) affects deformation and thrust. Keeping a consistent membrane area of 196 m^2, a thickness of 400 μm, and the properties of the polyimide material defined previously, we vary θ from 120 to 180 degrees, which allows us to explore the impact of a non-flat sail configuration on deformation, explicitly focusing on the Parachute-folded sail design. Fig. 17 illustrates a significant increase in the deformation as the sail approaches flatness (θ close to 180 degrees). Our Finite Element Method (FEM) results also provide thrust values corresponding to different θ angles.

These findings show that the deformation remains low until θ reaches approximately 175 degrees. Beyond this point, the deformation increases exponentially. The thrust graph indicates that around $\theta = 170$ degrees, the thrust approaches that of the flat sail ($\theta = 180$ degrees). To mitigate the exponential increase in deformation while maintaining high thrust, we selected $\theta = 170.18$ degrees as a promising candidate to optimize our Parachute-folded sail design. The fold's comparable maximum height at this angle is 0.1 meters. A larger value of θ minimizes deformation while maintaining a thrust comparable to that of the flat sail.

Having chosen the optimal θ for maximum performance, we now reduce the sail's thickness to decrease the overall mass and enhance characteristic acceleration. To ensure that these reductions do not compromise the sail's integrity, we also explore the impact of reinforcing the sail's outer borders to improve structural stability and performance.

7. Optimization of parachute-folded sail solar sail design

This section outlines the optimization process for the Parachute-folded sail solar sail design, focusing on reducing thickness, integrating reinforcement materials, and analyzing the impact on deformation, mass, and moment reactions. All results are based on the sail membrane area of 196 m^2.

7.1. Solar Sail Deformation for different thickness

To compare the performance of a Parachute-folded sail with that of a flat sail, particularly in terms of deformation due to solar radiation pressure (SRP), we conducted simulations using a Parachute-folded sail with a height of 0.1 meters. The deformation values for sail thicknesses ranged from 30 μm to 400 μm.

Given the need to compute multiple thicknesses for comparison, the computational time increased significantly. Parachute-folded sails were modeled with a quarter of their original geometry to reduce computational cost. Symmetry regions were defined within the software, leveraging the geometric symmetry of the sails, as well as the symmetry of their supports and loading conditions. To guarantee that the symmetry was applied correctly, we confirmed that the deformation values were kept around the same as those of the previous simulations with full model sails.

Across the range of 30 μm to 400 μm, the Parachute-folded sail consistently exhibited lower average deformation than the 400 μm thick flat sail. To achieve the same maximum deformation as the 400 μm flat sail, the equivalent thickness for the Parachute-folded sail would be approximately 130 μm. These results can be observed in the Fig. 18.

The 30 μm thickness represents a computational limit imposed by software constraints, while most solar sail projects use much thinner membranes, typically around 7.5 μm or less. Currently, 4 μm membranes are widely available, and even thinner options (e.g., 2.5 μm and 0.9 μm) have been produced in small quantities for over a decade. This study aimed to demonstrate that Parachute-folded sails reduce deformation more effectively across various thicknesses. However, further investigation into configurations below 30 μm was not pursued due to convergence issues.

7.2. Thinner sail results in deformation patterns

Based on our previously shown results, we show in Fig. 19 the deformation patterns for flat and Parachute-folded sails for 400 μm, 50 μm, and 30 μm. We wanted to show the difference between the extreme results. How-

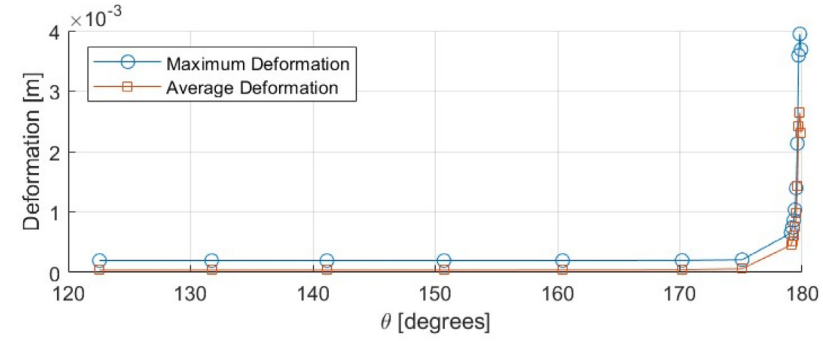

(a) Deformation depending on θ

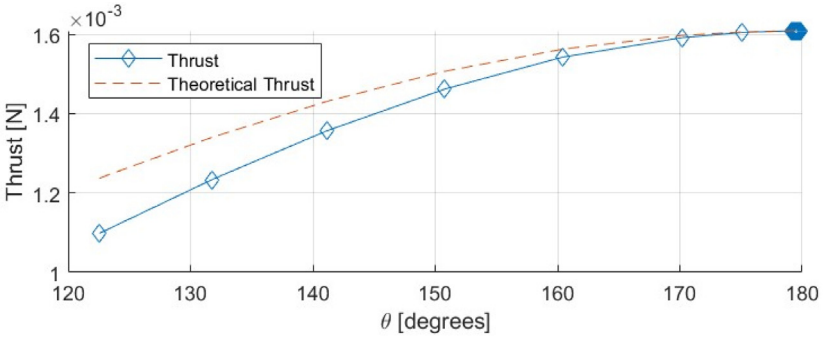

(b) Thrust depending on θ

Fig. 17. Deformation and Thrust for Parachute-folded sail with a thickness of 400 μm and an area of 196 m^2.

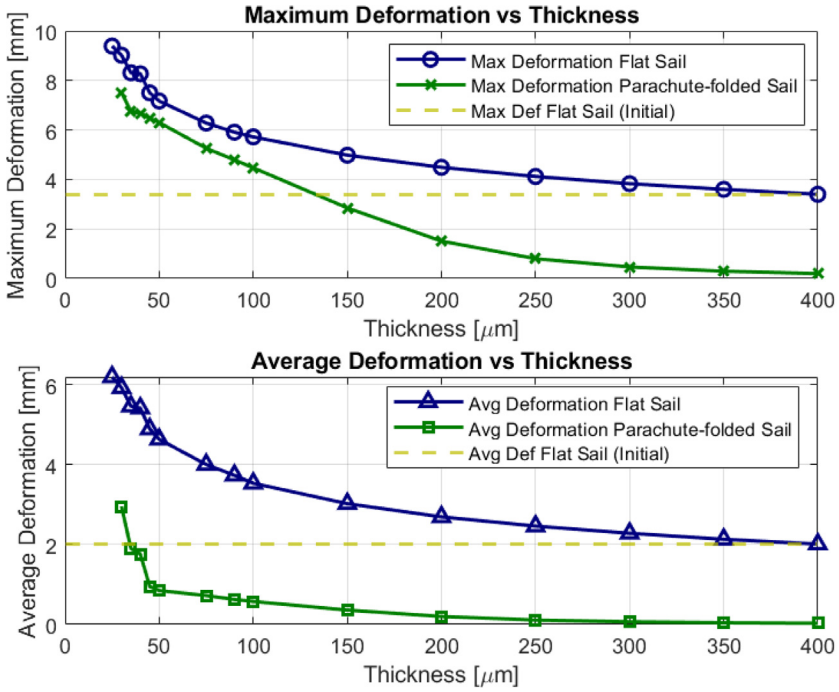

Fig. 18. Deformation values for various sail thickness, A $= 196\ m^2$.

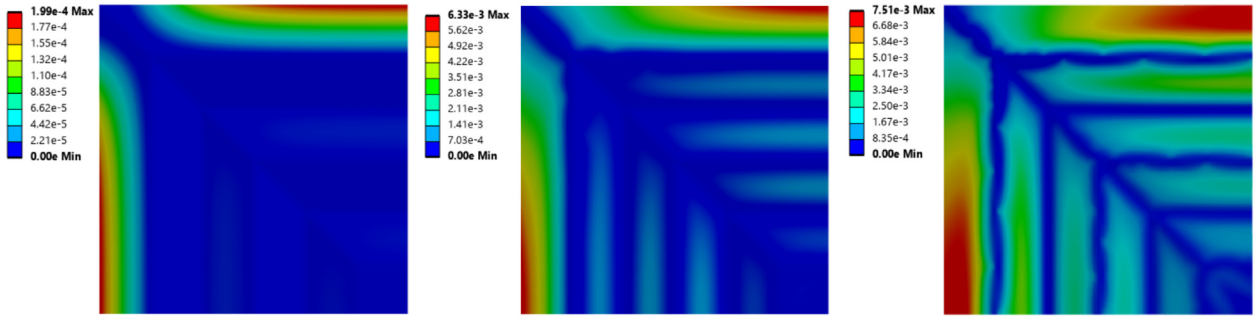

(a) Deformation in meters for thickness 400 μm (b) Deformation in meters for thickness 50 μm (c) Deformation in meters for thickness 30 μm

Fig. 19. comparison of deformation for the Parachute-folded sail with different thicknesses.

ever, the pattern for 50 μm was also included since, with this thickness, we observe a more prominent sail deformation on the Parachute-folded sail. Also, despite the reduction in thickness, the 50 μm thick Parachute-folded sail maintained an average deformation lower than the 400 μm flat sail, as shown in Table 7.

As it can be observed from the graphic in Fig. 18, for thicker and thinner sails, the Parachute-folded sail exhibits smaller average and maximum deformation than flat sails of the same thickness. Furthermore, looking at Fig. 19, the Parachute-folded sail maintains a deformation pattern across different thicknesses. In contrast, the thin, flat sails start showing more evident signs of wrinkling from the outer support to the sail's center, as seen in Fig. 20.

Also, it is interesting to consider that flat sails are initially folded before deployment, so even when they are supposed to become flat, the creases left on the sail could create a different deformation pattern. While flat sails are commonly used on missions, we can consider using non-flat sails to have a more consistent displacement pattern

Table 7
Comparison of deformation for Parachute-folded sail with reduced thickness to flat sail.

	Flat Sail			Parachute-folded sail		
Thickness [μm]	400	50	30	400	50	30
Maximum Deformation [m]	3.59×10^{-3}	7.49×10^{-3}	9.02×10^{-3}	1.99×10^{-4}	6.33×10^{-3}	7.51×10^{-3}
Average Deformation [m]	2.12×10^{-3}	4.89×10^{-3}	5.92×10^{-3}	2.88×10^{-5}	1.11×10^{-3}	2.95×10^{-3}

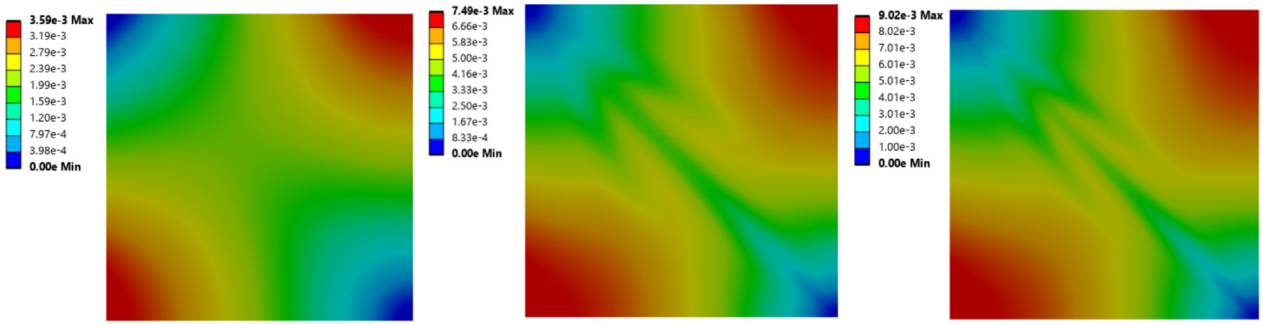

(a) Deformation in meters for thickness 400 μm (b) Deformation in meters for thickness 50 μm (c) Deformation in meters for thickness 30 μm

Fig. 20. comparison of deformation for the Flat sail with different thicknesses.

distribution while the sail is under the effect of SRP and smaller overall deformation.

8. Moment reaction analysis for non-perpendicular scenario

Building on our previous moment analysis, we further investigated the moment reactions in scenarios where the sun rays are not perpendicular to the sail surface. This assessment is crucial for understanding the sail's behavior under more realistic and varied solar orientations.

We conducted simulations to examine the moment reactions under different orientations of sun rays. All moment calculations consider the deformed shape of the sails. Initially, the sun rays were considered aligned with the z-axis ($\gamma = 0°$) as shown in Fig. 21a. Subsequently, the rays were inclined at 30 degrees by rotating counterclockwise about the XZ plane ($\gamma = 30°$), as illustrated in 21b. Considering the folded geometry, this inclination required recalculating the pressure distribution in the various areas of the Parachute-folded sail.

The pressure cannot be applied as an inclined vector to simulate that behavior in FEA because the sail is reflective, and the software does not account for those reflections. Therefore, the resultant pressure is first calculated on each fold and then applied perpendicularly to each fold. We then obtained the results for the moment reactions for the perpendicular and inclined scenarios for comparison.

We conducted simulations to evaluate the moment reactions for flat and Parachute-folded sails under different orientations of sun rays ($\gamma = 0°, \gamma = 15°$, and $\gamma = 30°$). Fig. 22 illustrates the moment reactions for these angles, comparing the results for thickness values of 100 μ m and 400 μ m.

As expected, the moment reaction for the flat sail decreases for sun rays approaching from an inclined direction because of the smaller equivalent pressure. However, for the inclined Parachute-folded sail, the absolute values of the moment increase due to the uneven pressure distribution. Additionally, thinner sails (100 μm) exhibited higher moment components due to their increased deformation compared to thicker sails (400 μm). This fact highlights the importance of optimizing sail thickness and fold design to balance deformation and moment reactions for effective solar sail performances.

To sum up, the study of moment reactions in non-perpendicular scenarios shows that flat sails experience reduced moments due to lower equivalent pressures from inclined sun rays. In contrast, Parachute-folded sails face increased moments due to the uneven pressure distribution.

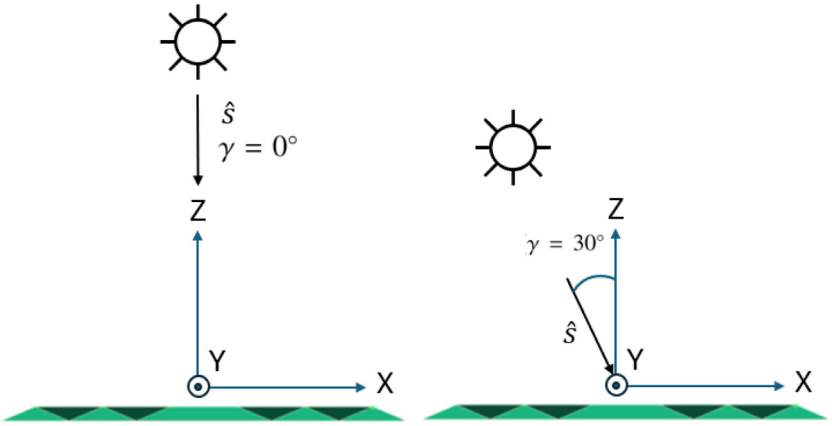

(a) Solar Rays perpendicular to the sail (b) Solar Rays inclined in respect to the sail

Fig. 21. Change of solar rays angle.

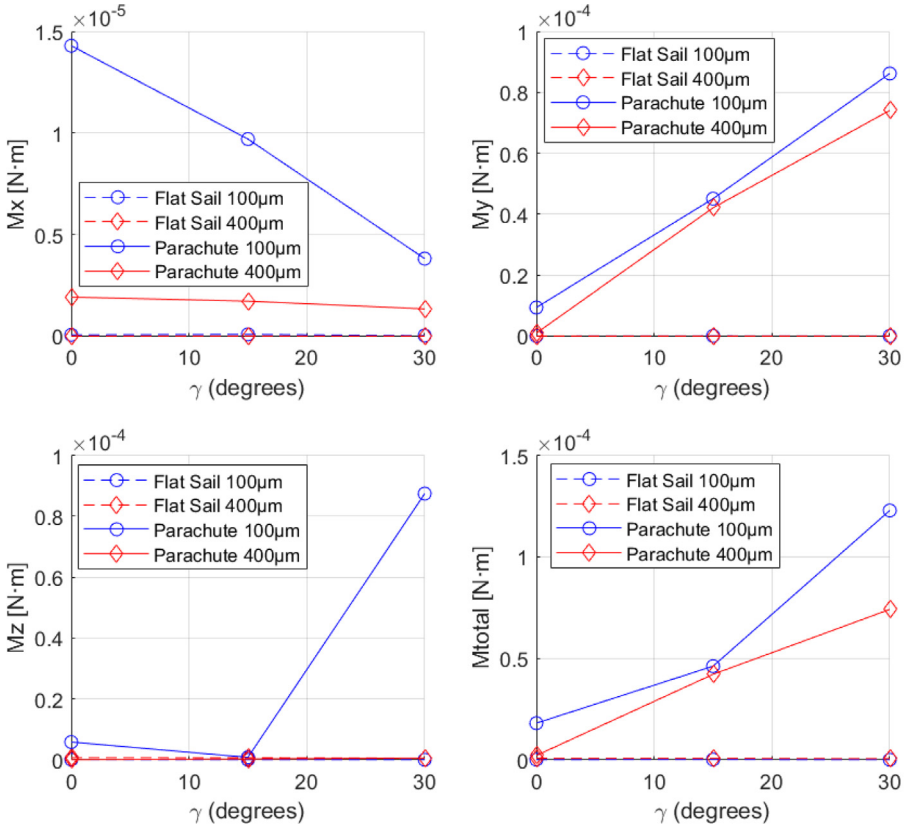

Fig. 22. Comparison of Moment Reactions for different angles ($\gamma = 0°, \gamma = 15°$, and $\gamma = 30°$).

Thinner sails exhibit higher moment components as a result of increased deformation. Therefore, while non-flat sails demonstrated smaller deformation values, they are expected to yield higher moment reaction values, especially when the sail is not perpendicular to the sun rays.

9. Characteristic acceleration comparison

Having systematically evaluated mass contributions, thrust capabilities, deformation characteristics, and moment reactions of various solar sail configurations, we now emphasize the characteristic acceleration (a_c) due to its pivotal role in mission feasibility and performance optimization.

To contextualize these findings, we incorporate data from the Nea Scout solar sail, which has an area of 80 m^2. For our 196 m^2 sail, additional masses, including booms and deployment systems, were estimated based on Nea Scout specifications with proportional scaling (Table 8). Despite their small relative masses compared to the sail film, these components contribute significantly to our comprehensive acceleration comparison (Diedrich, 2023).

Table 8
Extra masses for solar sail system.

Component	Mass [kg]
Deployment System	6.70
Bus	8.30
Booms	1.03
Total Extra Mass	16.03

Based on our previous deformation results for different sail thicknesses, we now include these additional masses to estimate our characteristic acceleration for a Parachute-folded sail and a flat sail with different thicknesses in Fig. 23. Thinner sails lead to lighter sails, which increases the characteristic acceleration but also increases deformation. The star point in the plot represents the reinforced Parachute-folded sail. For specific sail scenarios, we have the comparison in Table 9.

The deformation criteria determine how sail thickness affects characteristic acceleration. Very thin sails may be used if the deformation restrictions were loosened, which would lessen the impact of the deformation change while switching from flat to non-flat configurations. However, for strict deformation limitations, moderately thick sails, such as those with a thickness of 40 μm, show minimal deformation even without reinforcement, assuming rigid boom support. This result indicates a balance between achieving a higher characteristic acceleration and managing deformation risks. The results presented here provide a road map for optimizing the solar sail design by carefully balancing mass, thickness, and structural support to maximize the mission performance.

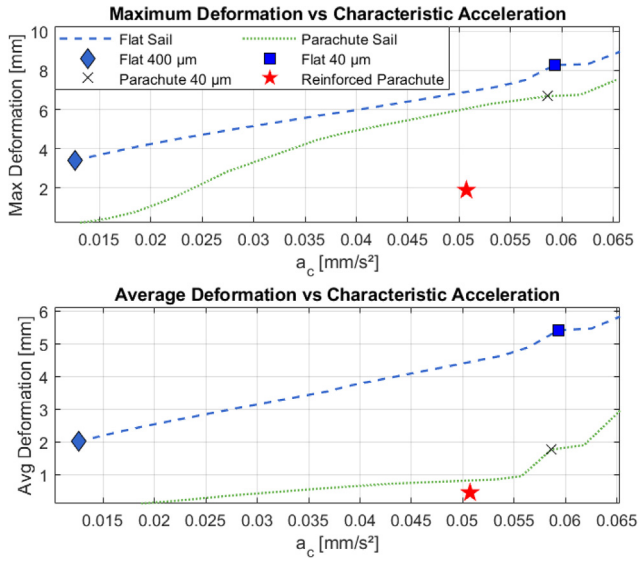

Fig. 23. Deformation vs Characteristic Acceleration, area 196 m^2.

10. Conclusion

This study thoroughly explores solar sail design and optimization, emphasizing its critical role in space exploration. We have made significant strides in enhancing the characteristic acceleration while maintaining the structural integrity and performance. Through detailed Finite Element Analysis (FEA) simulations, we investigated various folding techniques for non-flat solar sails, focusing on deformation patterns, thrust generation, and moment reactions, which provide valuable insights for future missions.

Among the techniques evaluated, the parachute-folded sail, reinforced with support points, demonstrated a superior performance characterized by a smaller, more symmetric deformation pattern. The strategic integration of reinforcement materials along the vulnerable outer edges of this sail significantly improved its structural stability. By adjusting the sail thickness and fold angles, we achieved an optimal balance among thrust, mass reduction, and average deformation.

A comparison between the final Reinforced Parachute-folded sail and the 400 μm thick flat sail highlights key improvements:

- **Characteristic Acceleration:** The flat sail reached a characteristic acceleration of 0.0126 mm/s^2, whereas the Reinforced Parachute-folded sail achieved 0.0507 mm/s^2, representing an increase of approximately 406%.
- **Mass Reduction:** The flat sail's film mass was 111.39 kg, while the Reinforced Parachute-folded sail reduced this to 15.39 kg.
- **Deformation:** The maximum deformation of the flat sail was 3.40×10^{-3} m, with an average deformation of 2.01×10^{-3} m. In contrast, the maximum deformation of the Reinforced Parachute-folded sail decreased to 1.90×10^{-3} m and the average deformation to 4.44×10^{-4} m.

Our findings indicate that the average and maximum deformations of the Parachute-folded sail consistently remained below those of flat sails in the thickness range of 30 μm to 400 μm. Although confirming a similar behavior in thinner sails would be beneficial, computational limitations imposed by boundary conditions - five support points, solar radiation pressure (SRP) at 1 AU, and no reinforcement - hampered the convergence for thinner sail models. Nevertheless, the non-flat sail configuration exhibits a substantial potential to maintain its structural integrity during flight without extensive reinforcement strategies.

Although using thinner sails would be advantageous for mass reduction, thicker sails offer significant benefits, particularly in mitigating the risk of overheating, an essential consideration for missions approaching the Sun, such as those targeting Venus or Mercury. Although flat sails are optimized for thrust and torque minimization, their practicality is limited by the need to fold them before deployment, which results in crease marks that can significantly affect post-deployment behavior. Therefore, assuming a fully flat sail in deformation analysis may not accurately represent real-world conditions, especially when reinforcements are applied along crease marks or tension cables are utilized to minimize film displacement.

Our moment reaction analysis also revealed that the Parachute-folded sail with 40 μm thickness and reinforced borders showed significantly reduced moment reactions compared to the 55 μm thick Parachute-folded sail with a similar film mass. The flat sail generated smaller moments across the evaluated thickness range of 100 μm to 400 μm, indicating further optimization opportunities to mitigate moment reactions and enhance structural stability. We also assessed moment reactions in non-perpendicular scenarios and found that the non-flat sail produced higher moments than the flat sail; however, this configuration remains promising without complicating attitude control.

Table 9
Masses, characteristic acceleration, and thickness comparison.

	Sail Film Mass [kg]	Total Mass [kg]	Thrust [N]	a_c[mm/s^2]	a_c%
Flat Sail (400 μm)	111.39	127.42	1.61×10^{-3}	0.0125	100%
Flat Sail (40 μm)	9.74	27.16	1.61×10^{-3}	0.0593	474%
Flat Sail (40 μm)	9.74	27.16	1.59×10^{-3}	0.0586	469%
Reinforced Parachute-folded sail (40 μm + 50 μm border)	15.39	31.42	1.59×10^{-3}	0.0507	406%

10.1. Future research

Future research should prioritize optimizing reinforcement strategies, exploring alternative folding techniques, and adjusting fold numbers to enhance sail performance. Additionally, evaluating the deformation of non-flat sails with thicknesses below 30 μm would allow for comparisons that align more closely with the performance of current thin-film solar sails.

A critical need is software capable of simulating membrane thicknesses down to 1 μm or even layered membranes. Solar sail membranes typically use 7.5 μm or 4 μm polymer films (e.g., Kapton, CP-1) coated with 100 nm metal layers (Al, Cr) for reflectivity. Advances in polymer technology are pushing membrane thicknesses to 2.5 μm and even 0.9 μm, though the metal coating still requires 100 nm to function as an efficient reflector. The metal layer occupies the outermost and most stressed layer and increases in importance as the thickness decreases, from approximately 2.5% to almost 20%. This change may significantly alter the material's properties, which could explain the software's current 30 μm limit.

This section outlines a comprehensive research opportunity for this team, other researchers, and software developers, establishing a foundation for further studies. Detailing this future work is essential as large membrane structures, especially for interplanetary missions, are often folded or rolled for extended periods before launch. In comparison, thin sails of 7.5 μm or less may behave similarly to flat, uncreased membranes; any folded or creased sail benefits from increased stiffness upon deployment. Intentional stiffening through fold lines, seam placement, or applied patterns could stabilize regions prone to deformation, preserving optimal reflection geometry and enhancing thrust control.

In conclusion, our theoretical analysis of non-flat sails across a limited thickness range offers promising insights into solar sail designs that incorporate necessary prelaunch folds. These concepts may be closer to practical application than initially anticipated.

Declaration of Competing Interest

The authors declare that they have no known competing financial interests or personal relationships that could have appeared to influence the work reported in this paper.

Acknowledgments

The authors thank their colleagues and peers for their invaluable feedback and discussions throughout this research. We also appreciate the support and resources provided by the Kyushu Institute of Technology.

References

Ancona, E., Kezerashvili, R.Y., 2017. Temperature restrictions for materials used in aerospace industry for the near-sun orbits. Acta Astronaut., 140, 565–569. URL: https://www.sciencedirect.com/science/article/pii/S009457651631308X. doi: 10.1016/j.actaastro.2017.09.002.

Baculi, J., 2016. Fuzzy Attitude Control of Solar Sail. Master's thesis Santa Clara University. URL: https://scholarcommons.scu.edu/cgi/viewcontent.cgi?article=1005&context=mech_mstr.

Berthet, M., Suzuki, K., 2023. Sunflower mission concept for high-altitude earth observation in leo via nanosatellite with pyramidal solar sail. Acta Astronaut., 213, 516–536. URL: https://www.sciencedirect.com/science/article/pii/S009457652300471X. doi:10.1016/j.actaastro.2023.09.017.

Block, J., Straubel, M., Wiedemann, M., 2011. Ultralight deployable booms for solar sails and other large gossamer structures in space. Acta Astronaut. 69, 78–85.

Boschetto, A., Bottini, L., Costanza, G., et al., 2019. Shape memory activated self-deployable solar sails: Small-scale prototypes manufacturing and planarity analysis by 3D laser scanner. Actuators 8 (2), 38.

Bovesecchi, G., Corasaniti, S., Costanza, G., et al., 2019. A novel self-deployable solar sail system activated by shape memory alloys. Aerospace 6 (7), 78.

Choi, M., 2015. Flexible Dynamics and Attitude Control of a Square Solar Sail Ph.D. thesis. University of Toronto, URL: https://tspace.library.utoronto.ca/bitstream/1807/69253/3/Choi_Mirue_201506_PhD_thesis.pdf.

Dachwald, B., 2010. Encyclopedia of aerospace engineering, pp. 1–14. https://doi.org/10.1002/9780470686652.eae292.

Diedrich, B., 2023. Solar sail torque model characterization for the near earth asteroid scout mission. In: Presented at The 6th International Symposium on Space Sailing.

Fernandez, J.M., Lappas, V.J., Daton-Lovett, A.J., 2011. Completely stripped solar sail concept using bi-stable reeled composite booms. Acta Astronaut. 69 (1–2), 78–85.

Grundmann, J.T., Boden, R., Ceriotti, M. et al., 2017. Soil to sail – asteroid landers on near-term sailcraft as an evolution of the gossamer small spacecraft solar sail concept for in-situ characterization. In: Proceedings of the 5th IAA Planetary Defense Conference – PDC 2017. Tokyo, Japan.

Johnson, L., Diaz, C., McNutt, L. et al., 2023. The NASA solar cruiser solar sail system–ready for heliophysics and deep space missions. URL.

Kezerashvili, R.Y., 2009. Thickness requirement for solar sail foils. Acta Astronaut., 65(3), 507–518. URL: https://www.sciencedirect.com/science/article/pii/S0094576509000939. doi: 10.1016/j.actaastro.2009.01.062.

Kezerashvili, V.Y., Kezerashvili, R.Y., 2024. Theoretical approach to circular solar sail deployment. Adv. Space Res., 73(9), 4731–4741. URL: https://www.sciencedirect.com/science/article/pii/S0273117724001315. doi: 10.1016/j.asr.2024.02.002.

McInnes, C., 1999. Solar Sailing: Technology. Dynamics and Mission Applications. Springer Praxis, London. https://doi.org/10.1007/978-1-4471-3992-8.

Miguel, N., Colombo, C., 2021. Deorbiting spacecraft with passively stabilised attitude using a simplified quasi-rhombic-pyramid sail. Adv. Space Res., 67(9), 2561–2576. URL: https://www.sciencedirect.com/science/article/pii/S0273117720302003. doi:10.1016/j.asr.2020.03.028.

Okuizumi, N., Yamamoto, T., 2009. Centrifugal deployment of membrane with spiral folding: experiment and simulation. J. Space Eng. 2 (1), 41–50. https://doi.org/10.1299/spacee.2.41.

Palmer, C., Shafer, J., 2004. Iso-area flasher. BARF AREA RAPID FOLDERS. URL: http://www.barf.cc/FlasherIsosimp.pdf.

Parque, V., Suzaki, W., Miura, S. et al., 2021. Packaging of thick membranes using a multi-spiral folding approach: Flat and curved surfaces. Adv. Space Res., 67(9), 2589–2612. URL: https://www.sciencedirect.com/science/article/pii/S0273117720306876. doi: 10.1016/j.asr.2020.09.040.

Price, H.W., Ayon, J., Garner, C. et al., 2001. Design for a solar sail demonstration mission. In: Space Technology and Applications

International Forum (STAIF-2001). Albuquerque, NM, USA: NASA Jet Propulsion Laboratory. URL: http://hdl.handle.net/2014/12303 jPL Clearance Number: 01-0335.

Satou, Y., Mori, O., Okuizumi, N., et al., 2015. Deformation properties of solar sail ikaros membrane with nonlinear finite element analyses. In: 2nd AIAA Spacecraft Structures Conference. https://doi.org/10.2514/6.2015-0436, URL: https://arc.aiaa.org/doi/abs/10.2514/6.2015-0436.

Satou, Y., Okuizumi, N., Sakamoto, H., et al., 2014. Nonflatness of solar sail membrane predicted by nonlinear finite element analyses. AIAA Spacecraft Structures Conference. https://doi.org/10.2514/6.2014-0832.

Schenk, M., Guest, S., 2010. Origami folding: a structural engineering approach. In: Proceedings of the 6th International Conference on Engineering, Science, and Technology, URL: https://www.researchgate.net/publication/265004670_Origami_Folding_A_Structural_Engineering_Approach.

Seefeldt, P., Dachwald, B., 2020. Temperature increase on folded solar sail membranes. Acta Astronaut. 177, 87–96. https://doi.org/10.1016/j.actaastro.2020.09.028.

Shirasawa, Y., Mori, O., Sawada, H., et al., 2012. A study on membrane deformation of solar power sail demonstrator ikaros. In: In 53rd AIAA/ASME/ASCE/AHS/ASC Structures, Structural Dynamics and Materials Conference. American Institute of Aeronautics and Astronautics, Reston, Virginia. https://doi.org/10.2514/6.2012-1747, URL: https://arc.aiaa.org/doi/abs/10.2514/6.2012-1747.

Sikes, J.D., Pezent, J.B., Rubinsztejn, A. et al., 2024. Off-nominal transfer analysis for nasa's solar cruiser mission. Acta Astronaut., 214, 53–63. URL: https://www.sciencedirect.com/science/article/pii/S0094576523005106. doi:10.1016/j.actaastro.2023.10.003.

Silverberg, J.L., Evans, A.A., McLeod, L., et al., 2014. Using origami design principles to fold reprogrammable mechanical metamaterials. Science 345 (6197), 647–650. https://doi.org/10.1126/science.1252876, URL: https://www.science.org/doi/abs/10.1126/science.1252876. arXiv:https://www.science.org/doi/pdf/10.1126/science.1252876.

Spencer, D.A., Betts, B., Bellardo, J.M., et al., 2020. The lightsail 2 solar sailing technology demonstration. Adv. Space Res. 66. https://doi.org/10.1016/j.asr.2020.06.029.

Takao, Y., Mori, O., Matsushita, M., et al., 2021. Solar electric propulsion by a solar power sail for small spacecraft missions to the outer solar system. Acta Astronaut. 181, 362–376.

Vulpetti, G., Johnson, L., Matloff, G., 2008. Solar Sails - A Novel Approach to Interplanetary Travel. Copernicus Books.

Wang, J., Nie, Y., Yuan, H. et al. (2024). Thermal-structural and prestressed modal analyses for a solar sail with nonlinear shape memory alloy spring. Adv. Space Res., 74(4), 1770–1780. URL: https://www.sciencedirect.com/science/article/pii/S0273117724004885. doi: 10.1016/j.asr.2024.05.047.

Yo, A., 2021. From origami to ikaros - jaxa. JAXA Education Center., URL: https://edujaxa.jp/activities/SEEC/material/assets/SEEC27-yo.pdf.

Zhao, P., Wu, C., Li, Y., 2023. Design and application of solar sailing: A review on key technologies. Chin. J. Aeronaut., 36(5), 125–144. URL: https://www.sciencedirect.com/science/article/pii/S1000936122002564. doi:10.1016/j.cja.2022.11.002.